Plasma Detachment Study of High Density Helium Plasmas in the Pilot-PSI Device

Y. Hayashi*[1], K. Ješko[2,3], H.J. van der Meiden[3], J.W.M. Vernimmen[3], T.W. Morgan[3], N. Ohno[1], S. Kajita[4], M. Yoshikawa[5] and S. Masuzaki[6]

[1]*Graduate School of Engineering, Nagoya University, Nagoya, Aichi 464–8603, Japan*

[2]*CEA, IRFM, F–13108 Saint–Paul–Lez–Durance, France*

[3]*FOM Institute DIFFER – Dutch Institute for Fundamental Energy Research, partner in the Trilateral Euregio Cluster, Eindhoven, the Netherlands*

[4]*Institute of Materials and Systems for Sustainability, Nagoya University, Nagoya, Aichi 464–8603, Japan*

[5]*Plasma Research Center, University of Tsukuba, Tsukuba, Ibaraki 305–8577, Japan*

[6]*National Institute for Fusion Science, Toki, Gifu 509–5292, Japan*

Corresponding author E-mail: hayashi-yuki13@ees.nagoya-u.ac.jp

Abstract. We have investigated plasma detachment phenomena of high-density helium plasmas in the linear plasma device Pilot-PSI, which can realize a relevant ITER SOL/Divertor plasma condition. The experiment clearly indicated plasma detachment features such as drops in the plasma pressure and particle flux along the magnetic field lines that were observed under the condition of high neutral pressure; a feature of flux drop was parameterized by using the degree of detachment (DOD) index. Fundamental plasma parameters such as electron temperature (T_e) and electron density in the detached recombining plasmas were measured by using different methods: reciprocating electrostatic probes, Thomson scattering (TS), and optical emission spectroscopy (OES). The T_e measured by using single and double probes corresponded to the TS measurement. No anomalies in the single probe *I-V* characteristics, observed in other linear plasma devices [16,17,36], appeared under the present condition in the Pilot-PSI device. A possible reason for this difference is discussed by comparing the different linear devices. The OES results are also compared with the simulation results of a collisional radiative model. Further, we demonstrated more than 90% of parallel particle and heat fluxes were dissipated in a short length of 0.5 m under the high neutral pressure condition in Pilot-PSI.

PACS numbers: 52.70.Nc, 52.70.Kz, 52.25.Xz, 52.55.Rk

Submitted to: *Nuclear Fusion*

1. Introduction

Handling enormous plasma heat and particle loads to divertor plates is essential to the achievement of high fusion gain in magnetically confined fusion. In ITER with fusion power (P_{fus}) of 500 MW, most of the exhausted power crossing the separatrix from the core (P_{SOL}) of ~ 100 MW must flow along open field lines in the scrape-off layer (SOL) connecting directly to the divertor target plates [1, 2]. Assuming P_{fus} ~ 3 GW class DEMO fusion reactor with the ITER-size plasma, P_{SOL} is expected to be ~ 500 MW [3]. On the other hand, the technologically feasible capability for heat handling of the divertor is typically 10 MW m^{-2} for an actively cooled structure in ITER [4], while in DEMO it could be below 10 MW m^{-2} due to neutron irradiation effects [5–7]. Consequently, a radiative divertor scenario should be developed to reduce P_{SOL} below 50 MW handled by total heat sink in divertors, where a radiation loss fraction (P_{rad}/P_{SOL}, P_{rad} is radiation power) of larger than 50% in ITER and 90% in DEMO is required in edge and divertor regions [8, 9].

The plasma heat flux q to the divertor plate is simply described by:

$$q = \Gamma[\gamma' T_e + E_i], \quad (1)$$

where Γ is the particle flux to the divertor plate, T_e is the electron temperature, γ' is the effective energy transmission factor through the sheath and E_i is the surface recombination energy corresponding to the ionization potential energy, respectively [3, 10]. Because ions have an intrinsic ionization potential energy E_i, which is released on the divertor plate due to the surface recombination process, simple cooling of the kinetic plasma energy T_e is insufficient for the reduction of the heat load onto the divertor plate. Therefore, the electron-ion recombination (EIR) process, including radiative and three body recombination, is required to dissipate Γ and reduce q. In plasma detachment physics, especially, detailed investigation of detached recombining plasmas associated with the EIR process is required to control the heat load to the divertor plate. In addition to the EIR process, the effects of radial/anomalous transport in the private and SOL regions also contribute to Γ reduction, leading to q reduction [11].

Linear plasma devices are able to simulate the open magnetic field geometry from the SOL to the divertor plate in magnetically confined fusion devices, and various experiments in detached recombining plasma are possible due to their experimental flexibility compared to fusion devices. So far, linear plasma devices have contributed significantly to understanding the mechanisms of plasma detachment [12]. For example, experimental proofs for volumetric recombination processes in helium and helium-hydrogen mixture plasmas [13–15], anomalous characteristics of single Langmuir probes in detached recombining plasmas [16,17], and plasma fluctuations associated with non-diffusive radial transport [18,19] were observed in NAGDIS-II. An observation of hydrocarbon-enhanced molecular activated recombination (MAR) processes [20] and detailed measurements of recombining plasma parameters by using a laser Thomson scattering (TS) system and a high-resolution spectrometer

[21,22] were performed in MAP-II. In TPD-SheetIV, experiments with a V-shaped target in detached hydrogen sheet plasma were performed [23], and direct observations of hydrogen molecular ions (such as H_2^+ and H_3^+) with an omegatron mass-analyzer were also carried out to understand dissociative recombination processes in MAR [24]. The neutral pressure dependence of vibrational, rotational, and kinetic temperatures of hydrogen molecules [25] and helium atom emission from an ionized cylindrical plasma with a recombining edge [26] was measured in PISCES-A.

Additional studies on plasma detachment in more relevant divertor plasma conditions with high density and high particle flux are required for demonstrating the effectiveness of plasma detachment in next-generation fusion devices such as ITER and DEMO. Further, in the ITER research plan, initial studies of H-modes and ELM control are planned in helium plasmas because the predicted H-mode threshold power in helium plasma is lower than that of hydrogen [27]. In helium plasma, the higher heat flux due to surface recombination than hydrogen is expected, because of its high ionization potential energy (24.6 eV). Therefore, it is also necessary to conduct plasma detachment experiments under the high-density helium plasma condition that is relevant to detached divertor operations in ITER. The linear devices, Magnum-PSI and Pilot-PSI, which can generate high-density plasma ($> 10^{20}$ m^{-3}) and strong ion fluxes ($> 10^{24}$ ions $m^{-2}\,s^{-1}$), have been used for the many experiments from the viewpoint of plasma-material interactions [28–31]. The density reduction due to the volumetric recombination has been already found by using TS measurement in hydrogen plasma of Pilot-PSI [32]. However the fundamental study of detached recombining plasma such as momentum loss and plasma physics in high neutral pressure has not been sufficiently explored.

Secondly, resolution of the anomaly of Langmuir probe characteristics is crucial in plasma detachment studies. On divertor probe measurements in JET, the problem was highlighted with current-voltage (*I-V*) characteristics becoming distorted away from the conventional exponential curve during the high recycling and detached discharges [33,34]. The reduced ratio of the electron to ion saturation current was observed, which resulted in an overestimation of T_e. From the simulation results, the elevated non-Maxwellian tail was claimed to be the cause for overestimating T_e estimated by single probe [35]. The similar tendency was also observed experimentally in linear plasma devices. It was found that T_e obtained by using the single probe is much larger than that measured with optical emission spectroscopy (OES) in NAGDIS-II [16,17]. Measured T_e by using the single probe initially decreases with increasing neutral pressure and was found to saturate to be larger than 1 eV, and a further increase in neutral pressure correlated with an increase of T_e. In the detached recombining plasma in the NAGDIS-II, prominent continuum emission due to radiative recombination and line emissions from highly excited levels due to three-body recombination were clearly observed. This is therefore difficult to reconcile with T_e above 1 eV, because the three body recombination process dominates only for T_e below 1 eV. A similar anomaly in *I-V* characteristics was also observed in

MAP-II by comparing the electrostatic probe measurement to the TS measurement [36]. For a detailed investigation of this anomaly, additional experiments in other plasma devices are necessary. Also, detailed studies comparing electrostatic probes and other methods, such as the TS measurement, are required because the TS method can properly provide the local T_e.

In this study, in order to understand the fundamental properties of detached recombining helium plasma under more relevant ITER plasma conditions, the radial profiles of plasma parameters, such as T_e, and the electron density (n_e) have been measured in the Pilot-PSI device with reciprocating electrostatic probes, the TS measurement and OES, focusing on the neutral pressure dependence. Firstly the experimental results obtained by using these electrostatic probes were compared with those obtained by using the TS method and OES to determine the details of the probe anomaly. By comparing the plasma fluctuations in the linear plasma devices Pilot-PSI and NAGDIS-II, the mechanisms underlying the electrostatic probe anomaly are assessed. The evolution of the plasma pressure and flux drop along the magnetic field lines owing to momentum loss including the EIR process is also discussed, and the observed line emissions from the detached recombining plasmas are compared with the simulation results of a collisional radiative model. Finally, we investigate the parallel particle and heat fluxes in detached recombining plasmas in Pilot-PSI.

2. Experimental setup

The experiment was performed by using the Pilot-PSI [37] device, as shown in figure 1(a). The device consisted of a 1.2 m long and a 0.4 m diameter vacuum vessel that was placed inside five magnetic coils. The maximum magnetic field strength was 1.6 T at the vessel center. In this experiment, a DC cascaded arc produced a steady state helium plasma with a discharge current of 170 A and a discharge voltage of ~60 V. An axial magnetic field of 0.05 T confined and guided the plasma to the floating target that was located at $z \sim 560$ mm, where z is the distance from the plasma source. A gas flow was set to 2.5 standard liters per minute (slm). The neutral pressure (P) was monitored by using a baratron gauge on the top port of the machine above the target plate. By changing the pumping speed, P could be controlled (ranging from 4 to 18 Pa), while the plasma source parameters remained almost constant. Figure 2 shows the radial profiles of n_e and T_e at the upstream position ($z \sim 40$ mm) measured by using TS measurement during various P conditions. Although n_e profiles broadened slightly with P, the peak density did not change. This was because the low temperature (3–4 eV) meant that full ionization did not occur in all cases at column center, and in all cases the column profile is similar upstream regardless of P. Therefore, P was the key parameter for determining the detachment condition downstream. Here, we note that the pressure range from 4 to 18 Pa is higher than the detached plasma operations in other linear plasma devices, such as NAGDIS-II [38] and MAP-II [36]. However, it is similar to the detached condition expected in ITER [39]. The electrostatic probe was installed on the

horizontal port, 540 mm downstream from the source. TS measurement and OES were also performed at z ~ 540 mm (TS measurement was also carried out at z ~ 40 mm). The viewing systems of both diagnostics were set at the opposite port with respect to the electrostatic probe. The reciprocating electrostatic probe measurement was able to support the TS, especially in the plasma peripheral region, where the scattered light became weak.

Figure 1(b) shows the probe head designed for measuring T_e, n_e, ion saturation current (I_{sat}) and the floating potential (V_f) simultaneously. Four tungsten electrodes, numbered #1 to #4, with diameters of 0.5 mm were placed at the distance of 1.0 mm outside of an alumina rod. Electrodes #2 and #4 worked as single probes and together worked as a double probe oriented along the magnetic field lines. For the single probe and double probe measurements, the probe voltage V_p (a 50 Hz triangular wave, –70 V to 20 V for the single probes and –30 V to 30 V for the double probe, respectively) was applied by using a bipolar power supply. Considering the shadowing effect of the upstream electrode, the probe head was at an angle (θ ~ 15°) relative to the magnetic field lines. When bias voltages for electrodes #2 and #4 were fixed at –100 V, the probe drew the ion saturation current, I_{sat}. Electrodes #1 and #3 measured the V_f continuously. The sampling rate of the 12 bit A-D convertor was 5M samples/s for the single and double probes and V_f and 1M samples/s for I_{sat}. In the data acquisition system, the frequency response of probe current was 20 kHz. The reference potential for each probe tip was the vacuum vessel, and is referred to as the system ground. The anode of the cascaded arc was also grounded.

Figure 1(c) schematically shows the probe experiment. The probe head was horizontally driven by an electric motor at the constant velocity of 100 mm/s and swept in the plasma ~20 mm in front of the target plate (at z ~ 540 mm). As a result, radial profiles of the plasma parameters could be obtained.

3. Experimental results

3.1 Ion saturation current measurements

Figure 3(a) shows the neutral pressure (P) dependence of ion saturation current (I_{sat}) at the plasma center (radial position, r, of 0 mm) and far-peripheral position (r = –40 mm), measured by the electrostatic probe located at z ~ 540 mm. At r = 0 mm, I_{sat} decreased with increasing P. The strong decrease in plasma particle flux to the target at the center of the column is most likely due to recombination. However, at r = –40 mm, I_{sat} does not exhibit the strong reduction; moreover, I_{sat} slightly increases with increasing P. This result indicates that profile could be flattened at high P; and this tendency was also observed in NAGDIS-II [40]. Large error bars for I_{sat} at r = –40 mm indicates the large fluctuations in the peripheral region, because the error bars were based on standard deviation

of I_{sat}. Figures 3(b) and (c) show linear and logarithmic plots for radial profiles of I_{sat}, captured for the lowest (4 Pa), the intermediate (11 Pa), and the highest (18 Pa) values of P in this experiment. The radial profiles also reveal a dramatic reduction in the particle flux at the plasma center and profile flattening owing to the increasing P. The EIR process is more effective at the center of plasma column because high n_e leads to the enhancement of EIR [41]. As shown in figure 3(c), comparing the cases of the intermediate pressure (P = 11 Pa, square) and the lowest pressure (P = 4 Pa, circle), I_{sat} around $r <$ –20 mm for the intermediate P was larger than that for the lowest P, while the opposite was observed at r = 0 mm. This implies that the plasma density was slightly increased at periphery with increasing P. The possible reasons for the increase of density and flattening of the profile under the high P conditions are discussed in section 4.2.

3.2 I-V characteristics from the single probe and double probe measurements

Figure 4(a) shows the *I-V* characteristics for the single probe at r = 0 mm. By comparing the cases for the lowest P (left axis) and the highest P (right axis), it can be deduced that *I-V* characteristics are clearly different between the two cases. T_e was measured from the slope of the *I-V* characteristics on the logarithmic scale, as shown in figure 4(b). From the fit, we obtained T_e of ~1.5 eV and ~0.3 eV for the lowest and highest P cases, respectively.

Figure 5 shows the *I-V* characteristics for the double probe. The figure also shows a comparison between the lowest and highest P cases at r = 0 mm. Because special care was taken to sustain the electrical isolation between the double probe tips and the grounded area, the measured *I-V* characteristics were symmetric and the probe current, I_p, was almost zero when the V_p was zero. Analysis of the *I-V* characteristics of the double probe yielded a T_e of ~1.2 eV and ~0.35 eV for the lowest and highest P cases, respectively. The value of T_e measured by using the double probe was consistent with that measured by using the single probe. These results demonstrate that electrostatic probes can be used for high neutral pressure plasma in the Pilot-PSI system and for the experimental conditions described in section 2. It is interesting to note that this result contradicts the previously obtained results for other linear devices mentioned earlier, where anomalous probe measurements were observed to yield higher T_e in recombining plasma [16, 17, 36].

3.3 Comparison of electrostatic probes with Thomson scattering measurement

A Thomson scattering (TS) measurement system for measuring n_e and T_e was also installed in Pilot-PSI [42,43]. Figures 6(a) and (b) show the P dependence of n_e and T_e measured at r = 0 mm, with the double probe, single probe, and TS measurement at $z \sim 540$ mm. n_e measured by using the single probe and the double probe, monotonically decreased with P, while the TS measurement indicated a peak at $P \sim 8$ Pa. For the calculation of n_e, the ion saturation currents in the *I-V*

characteristics curves were used, and the probe surface area was set to a geometrical projection along the magnetic field lines by assuming a weakly magnetized plasma (actually, ion cyclotron frequency of ~ 0.2 MHz and ion–neutral collision frequency of ~ 1 MHz, when P ~ 4 Pa, i.e. the Hall parameter is 0.2). Considering the shadowing effect due to ion flow, only an upstream side of geometrical projection was used. Further, assuming that $T_i \sim T_e$ under the high density plasma condition, the ion sound speed of $C_s = (2T_e/m_i)^{1/2}$ was used in the calculations, where T_i and m_i are ion temperature and ion mass. Because of these assumptions, to quantitatively compare the n_e values that were measured by the electrostatic probes and TS, a careful estimation of the effective collection area of the probes is necessary. On the other hand, the value of T_e measured by both the single and double probes was in a good agreement with that measured by using TS. At $P < 10$ Pa, the reduction in T_e was steeper than that in n_e with increasing P, and T_e exhibited the lowest value (~ 0.2–0.4 eV) and was almost constant at $P > 10$ Pa. Although the double probe shows slightly higher T_e than that obtained by using other methods, it is difficult to compare T_e at $P > 10$ Pa because of the large error bars in T_e measured by double probe of ±0.2–0.4 eV.

Figure 7 shows the radial profiles of n_e and T_e at P values of ~ 4 and ~18 Pa, measured by using the double probe, the single probe and the TS measurement at $z \sim 540$ mm. At $P \sim 4$ Pa, n_e values determined by both electrostatic probes corresponded to that measured by using the TS, as shown in figure 7(a), and the radial profile of T_e measured by using the double probe was in a good agreement with that obtained by using the TS (figure 7(b)). At $P \sim 18$ Pa, both n_e and T_e exhibited flat profiles, as in figure 7(c) and (d). These results imply that with increasing P, the recombination dominantly starts at the center of plasma column and the plasma will diffuse across the magnetic field, corresponding to the results of I_{sat} measurement in figure 3. Again, it is worth noting that the electrostatic probes yielded a rather low temperature (below 1 eV) without any anomaly even at $P \sim 18$ Pa.

3.4 Optical emission spectroscopy

OES was also performed at $z \sim 540$ mm. The line of sight of an optical fiber was installed to pass through the plasma center. Figure 8 shows a typical spectrum of visible light emission in the 310–370 nm range, at $P \sim 9$ Pa. The emission from this recombining region exhibits a continuum radiation below ~ 344 nm into the 2^3P state and line emission of the 2^3P-n^3D series transitions. We can distinguish the line emission up to the principal quantum number $n \sim 16$. The continuum and line-series emissions from highly excited levels are due to the radiative and three-body recombination processes, respectively. These recombination processes mainly occur when the temperature is typically below 1 eV, and contribute to reducing the ion flux and heat load on the target.

In recombining plasmas, partial local thermodynamic equilibrium (pLTE) is satisfied above a certain quantum number. The population of atoms with highly excited levels obeys the Boltzmann

relation. In order to determine T_e by using spectroscopy, we used the Boltzmann plot method for a series of Balmer-type lines, which correspond to the transitions from highly excited levels to the $n = 2$ level, for helium atoms [15,45]. Figure 6(b) shows the T_e measured by using OES as a function of P and the results are compared with those obtained by using the probes and the TS. The T_e values measured by using OES are the lowest among the values obtained by using the different measurement techniques and exhibits a weak dependence on P, while T_e measured by using other methods decreases with increasing P. The apparently low central T_e obtained from the spectroscopy method is likely due to the line-integrated emission [26]. As shown in figure 6(b), at the low P (especially at $P \sim 4$ Pa), the largest difference of T_e between OES and other methods was observed. This is because the OES integrated the emissions along the line of sight, while other methods were localized at the plasma center. From the radial profile of T_e shown in figure 7(b), when $P \sim 4$ Pa, T_e measured by using OES of ~ 0.2 eV was obtained by combining emissions from the $T_e \sim 1.2$–1.5 eV core and the $T_e \sim 0.2$ eV halo around the core. In general, line spectra due to three-body recombination are dominated by emissions from the low T_e and high n_e region, because the EIR process strongly depends on n_e and T_e. In the present study, measured T_e by using OES is affected by the low T_e recombining edge plasma, especially during low P operation.

4. Discussion

4.1 Influence of plasma fluctuations on the probe measurements

In this section, the effect of fluctuations on the probe measurements in detached recombining plasmas is discussed. A large plasma fluctuation was pointed out as one of the reasons for overestimation of T_e in recombining plasmas of NAGDIS-II and MAP-II [17,36]. Figures 9(a) and (b) show the fluctuation levels of I_{sat} and V_f as a function of radial position, comparing between the typical recombining plasmas in the NAGDIS-II and Pilot-PSI devices. Here, the fluctuation levels are defined as $\left\langle \tilde{I}_{sat}^2 \right\rangle^{1/2} / \left\langle I_{sat} \right\rangle$ for I_{sat} and $\left\langle \tilde{V}_f^2 \right\rangle^{1/2} / T_e$ for V_f, respectively, where $\langle\ \rangle$ indicates the time-averaging and superscript ~ denotes the fluctuation component obtained by subtracting the mean value $\left\langle I_{sat} \right\rangle$ and $\left\langle V_f \right\rangle$ from the original I_{sat} and V_f. It is known that I_{sat} is proportional to $n_e T_e^{1/2}$, and that V_f can be expressed as $V_f = V_s - \alpha T_e$, where α is a constant. It is assumed that $\tilde{V}_f \sim \tilde{V}_s$ in the detached recombining plasma because $\tilde{T}_e$ is small due to small T_e values. Therefore, fluctuation of I_{sat} and V_f are mainly determined by the density and potential fluctuations, respectively. The magnetic field strength and P were 0.15 T and 2 Pa in NAGDIS-II, while they were 0.05 T and 9 Pa in Pilot-PSI. As shown in figure 9(a) and (b) both the density and the potential fluctuation levels

were much higher for NAGDIS-II than for Pilot-PSI. It was considered that the plasma potential fluctuation especially affects the probe *I-V* characteristics [14]. Figure 10 schematically shows the influence of plasma potential fluctuation on the single probe *I-V* characteristics. The slope of the time-averaged *I-V* curve obtained in the experiments might not be changed when the amplitude of $\tilde{V}_s$ is much less than T_e. However, when the amplitude of $\tilde{V}_s$ extends to the saturation region, the slope of the time-averaged *I-V* curve is varied to give higher T_e because the *I-V* curve is rounded by the influence of the plasma potential fluctuation. As shown in figure 9(b), the difference of potential fluctuation level normalized by T_e between NAGDIS-II and Pilot-PSI was more than one order of magnitude at the center and approximately one order of magnitude on the periphery. Moreover, the amplitude of the fluctuating component $\left\langle \tilde{V}_f^2 \right\rangle^{1/2}$ is ten times larger than T_e in NAGDIS-II, while it was less than T_e in Pilot-PSI.

In the present study, it was shown that T_e was properly measured even in the recombining plasmas without any anomaly of probe *I-V* characteristics. In the past experiments in NAGDIS-II and MAP-II, however, the anomalous probe measurements resulted in an overestimation of T_e in the recombining plasma [16,17,36]. By comparing the fluctuations in NAGDIS-II and Pilot-PSI, it was found that the plasma fluctuations could be a significant factor affecting the probe measurement, especially the T_e analysis. From the present results, it can be also said that anomaly of Langmuir probe characteristics are not necessarily observed in detached plasmas, especially at low fluctuation levels.

It was reported that an intermittent density fluctuation is frequently produced near the recombination front in detached recombining plasma in NAGDIS-II [46]. This result suggests that the recombination front, which exists in the transition region from the ionizing plasma to the recombining plasma, might be the fluctuation source. In the present study, on the other hand, the transition region similar to the recombination front was not observed in Pilot-PSI. It could be considered that the high density plasma upstream led to the strong recombination process, although $T_e \sim 3$–4 eV at the center. In other experimental conditions such as hydrogen discharges or in low density plasma, however, the fluctuation level might be larger because of the existence of ionizing plasma as well as a recombination front in upstream. This hypothesis should be investigated in more detail. In order to reveal the behavior of plasma instabilities, further experiments and theoretical studies are needed. In addition, it was also reported that the non-Maxwellian tail strongly affects the plasma diagnostics [35]. The effect of velocity distribution function on electrostatic probe measurements should be also investigated under the detached recombining plasma conditions.

4.2 Intermittent radial transport

Experimental results indicated that plasma density profile became flat in high *P* operation as shown in

I_{sat} profiles in figure 3 and n_e profiles in figure 7. Although the reasons to cause this tendency are not currently clear, we speculate that one possibility is intermittent cross-field transport as observed in other linear magnetized plasmas [18,19,46–48]. This is similar to transport associated with plasma blobs occurring in magnetically confined fusion devices [49–51]. Intermittent radial transport, having a higher density than the ambient plasma in the peripheral region, is transported convectively by the centrifugal force of plasma rotation or the effect of a neutral wind, which is generated by a charge exchange process in the plasma column [52]. These drive mechanisms in linear plasma devices are different from those in fusion devices. Tanaka et al. [18] reported detailed analytical analysis on 2D motion of spiral structures in peripheral regions across the magnetic field under detached recombining plasma conditions in NAGDIS-II. These structures were radially localized and propagated far from the plasma column, increasing the ambient plasma density.

A possible reason causing the similar broadening of the plasma profile here could be such intermittent radial transport. However, intermittent radial transport was especially enhanced during the transition from attached to detached plasma [40], and some other reasons might be considered, e.g. diffusive and anomalous transport in a radial direction and the effect of radiation transport. For example, radiation from the central region should be trapped by ground state and enhance the population of the singlet system at the peripheral region [53], and result in increasing n_e due to the low ionization energy of excited neutrals. Many highly excited neutrals produced in high density center are also candidates for causing broad profile, because they become free from the magnetic confinement immediately after the recombination and increase n_e in the periphery like the radiation transport.

4.3 Pressure balance

In order to quantitatively compare the observations described in the previous section, the extent of plasma detachment has to be defined numerically. For this purpose, the concepts of "pressure balance" and "degree of detachment" are introduced. The pressure balance is explained in section 4.3, and the degree of detachment is explained in section 4.4.

Assuming no pressure/momentum source or loss in a flux tube, the static pressure component $n_eT_e + n_iT_i$ plus the dynamic pressure component $n_im_iv^2$ should be constant along the magnetic field lines, where n_i, T_i, m_i, and v are the ion density, ion temperature, ion mass, and flow velocity. When $T_e = T_i$ and $n_e = n_i$ are assumed in the high-density plasma of Pilot-PSI, the plasma static pressure is $2n_eT_e$. At the sheath edge, v should be ion sound speed $C_s = (2T_e/m_i)^{1/2}$. Based on the OES analysis of Pilot-PSI, it was measured that velocities at the source can be approximately $0.2C_s$ [54]. Thus, the relation between the static and dynamic pressures at the downstream and upstream is,

$$n_d(2T_d + 0.2^2 m_i C_{sd}^2) = n_u(2T_u + 0.2^2 m_i C_{su}^2), \quad (2)$$

where the subscripts "d" and "u" denote the downstream and upstream location, respectively. It was

assumed that the flow velocity at the downstream position was also 0.2 C_s. The sheath edge was located much closer to the target plate in comparison with the distance between the probe and the target plate (20 mm). Sheath thickness was 1.5×10^{-5}m given by 10 times larger than the Debye length under the condition that $n_e \sim 5\times10^{18}$m^{-3} and $T_e \sim 0.2$ eV. Eq. (2) therefore becomes,

$$n_d T_d = n_u T_u . \tag{3}$$

Eq. (3) prescribes that the static plasma pressure is conserved along the magnetic field lines. On the other hand, in general tokamak SOL physics, static plasma pressure will drop by half during the transport from the upstream location to the target. This follows because the upstream location, where ionization collisions are dominant and the dynamic pressure is negligible, is characterized by $v = 0$, i.e. a so called stagnation point [55,56].

Figure 11(a) shows the P dependence of the plasma pressure, which is estimated as the averaged n_eT_e at different positions along the magnetic field. The quantities $\langle P_d \rangle$ and $\langle P_u \rangle$ are the radial averaged plasma pressure over the center of the plasma column obtained from n_e and T_e measured by the TS at the downstream ($z \sim 540$ mm) and at the upstream location ($z \sim 40$ mm), respectively. Here, a radial average over the center of the plasma was calculated by using the following formula,

$$\langle P_t \rangle \& \langle P_u \rangle = \frac{1}{S}\int_0^{2\pi}\int_{0\text{mm}}^{10\text{mm}} n_e(r)T_e(r) r\,\mathrm{d}r\,\mathrm{d}\theta , \tag{4}$$

where S is the area of a circle with the radius of 10 mm in the plasma, where 10 mm is the approximate half width at half maximum (HWHM) of the n_e profile obtained by using the TS measurement. Eq. (4) assumes the profile to be rotationally symmetrical. In figure 11(a), $\langle P_d \rangle$ monotonically decreases with increasing P, while $\langle P_u \rangle$ remains almost constant. Figure 11(b) shows the $\langle P_d \rangle$ to $\langle P_u \rangle$ ratio. As shown in eq. (3), which assumes the conservation of the static pressure plus dynamic pressure, $\langle P_d \rangle$ should be comparable to $\langle P_u \rangle$. However, the measured ratio is ~0.25 at $P \sim 4$ Pa, corresponding to the lowest P in this experiment. Furthermore, the ratio continues to decrease with increasing P, up to < 0.01. The result is unexplainable without assuming the loss of momentum along the magnetic field lines, because the plasma pressure is not conserved. Under the condition of a high neutral pressure, a reduction in the plasma pressure can be induced by the momentum losses owing to ion-neutral collisions, including charge-exchange and EIR processes. The experimental results were also unexplainable by eq. (3) even at low P conditions. Because the emission due to the EIR was observed when $P \sim 4$ Pa, the recombining plasma appears to already exist at low P in front of the target plate. The EIR as well as the charge exchange might also contribute to

the pressure drop between upstream and target in low P conditions.

4.4 Degree of detachment

The reduction in the ion flux into the target is one of the characteristic observations defining detachment. A useful concept for quantitatively understanding the onset and extent of the detachment is the degree of detachment (DOD) [56–58], defined as,

$$\mathrm{DOD} = \phi_{\mathrm{calculated}} / \phi_{\mathrm{measured}}, \tag{5}$$

where ϕ_{measured} is the measured ion flux onto the target by the electrostatic probes, and,

$$\phi_{\mathrm{calculated}} = C n_{\mathrm{u}}^2, \tag{6}$$

is calculated by extrapolating the ion flux onto the attached target. Eq. (6) is based on the prediction of the basic two-point model,

$$\Gamma_{\mathrm{t}} \propto n_{\mathrm{u}}^2 q^{-3/7} L^{4/7}, \tag{7}$$

where Γ_{t} is the ion flux onto the target, q is the heat flux, and L is the connection length. C is the normalization constant, which is obtained experimentally from the ion flux measured by using the electrostatic probes. Generally, in the experimental devices such as JET, C is obtained during the attached phase of discharge [57,58]. In this study, C was chosen by using the ion flux at $P \sim 4$ Pa, the lowest P. The quantity n_{u} is the electron density measured by using the TS in the upstream region. Therefore, $\phi_{\mathrm{calculated}}$ could be estimated under the present experimental conditions. The ϕ_{measured} was estimated from the I_{sat} measured by using the electrostatic probes 20 mm in front of the target, because the flux measurement was not conducted at the target plate.

Figure 12(a) shows the P dependences of $\phi_{\mathrm{calculated}}$ and ϕ_{measured}. The quantity ϕ_{measured} decreases with increasing P, although $\phi_{\mathrm{calculated}}$ did not decrease. The ϕ_{measured} was calculated from I_{sat} profile by using same radial averaging procedure expressed in eq. (4). The reduction of ion flux was likely due to the decrease of T_{e}, leading to enhanced recombination. Other processes that can also lead to decreased ion flux are: a lower flow velocity at low T_{e}, higher neutral pressures, which impede the ion flow through ion-neutral collisions, including charge exchange. Lastly, a drop in particle source (ionization in the plasma between the upstream and the recombination region) can also lead to a drop in ion flux. As shown in figure 12(b), the DOD increases with increasing P. As described in section 4.3, the EIR process is dominant even for 4 Pa. These results quantify the further detachment with increasing P.

In addition to the plasma pressure (described in section 4.3), the ion flux also decreased. This, too, was likely caused by the momentum loss. Momentum loss is one of the characteristics of plasma detachment [38, 59, 60]. Figure 13 shows a schematic illustration of the formation of detached helium

plasma and axial profiles of n_e and T_e under high neutral pressure. The figure describes the transition from a radiation region to a recombination region in the divertor plasma of a fusion device. The major mechanisms of the electron energy loss are the ionization and radiation processes at T_e above 5 eV. However, when T_e is below 5 eV, the energy relaxation between electrons and ions becomes the dominant electron energy loss channel instead of the ionization and radiation processes, because the electron-ion energy relaxation time is proportional to $T_e^{3/2}$. The ions lose their energy in charge-exchange and ion-neutral elastic collisions. These processes make the ions and electrons sufficiently cold. Below T_e < 1eV, the EIR process become dominant. In the Pilot-PSI operation, the neutral and plasma species densities are high. Therefore, the ion energy is decreased by interactions with neutral particles, and the electrons and ions are strongly coupled through the energy relaxation process. The plasma pressure and the particle flux drops along the magnetic field lines were observed at high neutral pressure owing to these momentum loss processes, including the EIR and charge-exchange processes. Further, the EIR process mainly affects the momentum losses in the case of low T_e, typically T_e < 1 eV, because the rate coefficients for the EIR process strongly depend on T_e while charge-exchange exhibits a weak dependence on the temperature. Because T_e in the upstream region is < 5 eV, in this experiment, the detached helium plasma was mainly determined by the electron-ion energy relaxation process, as shown in the last half of figure 13.

4.5 Comparison with the collisional radiative model

In order to understand the fundamental properties of atomic processes in the Pilot-PSI system, the He–I lines from low–*n* and high–*n* states were compared. As well as T_e estimation by using OES, the line of sight of an optical fiber was installed to pass through the plasma center at $z \sim 540$ mm. Under the present experimental conditions, because T_e was below 1.5 eV in front of the target, the population of high–*n* states was likely to be determined by the EIR process. In recombining plasma, the transitions from highly excited levels are the indications of EIR. Figure 14 shows the P dependences of the low–*n* He–I (471.3 nm: 2^3P–4^3S) emission, the high–*n* He–I (355.4 nm: 2^3P–10^3D) emission, and the ratio of 355.4 nm /471.3 nm. Both the low–*n* and high–*n* emissions exhibit a peak at $P \sim 9$ Pa and decrease gradually with increasing P. Regarding the high–*n* emission, the increase up to $P \sim 9$ Pa could be due to enhancement of the EIR process and the decrease by the extinction of plasma. When the population of low–*n* states is primarily filled up with the electrons excited from the ground state, the low–*n* emission should depend on n_e and decrease with increasing P. However, both low–*n* and high–*n* emissions exhibit similar tendencies. Moreover, the ratio gradually reduces with increasing P, indicating that the EIR rate decreases. Owing to the steep reduction in T_e and the enhancement of the EIR process, the assumption that low–*n* state population depends on the excitation from the ground level is not realistic.

Here, in order to investigate the transition rate into the 4^3S excited state caused by the EIR and excitation processes, a collisional radiative (CR) model for neutral helium was applied [61,62]. In this model, the densities of the various excited states of a specific atom or ion can be calculated as the outputs of relevant input parameters, such as the ground state (1^1s) density, n_0, the ion density, n_i, T_e, and n_e. The population density of the level p, $n(p)$, is calculated by considering the coupling with other levels (spontaneous transition and electron impact transition of excitation or de-excitation), electron impact ionization and recombination. In many cases, the relaxation time of the excited level population is sufficiently short, compared with the time constants for changes in T_e and n_e, so that the time derivative of $n(p)$ can be approximately zero. When this quasi-steady-state approximation is valid, the simultaneous equations for all of the excited levels can be easily solved, and the quantity $n(p)$ can be expressed as a sum of two terms,

$$n(p) = n_0(p) + n_1(p) = R_0(p) n_e n_i + R_1(p) n_e n_0 . \quad (8)$$

The coefficients $R_0(p)$ and $R_1(p)$ are the functions of T_e and n_e and are called the reduced population coefficients. $R_0(p)$ and $R_1(p)$ are calculated as the results of CR model and reflect the collisional and radiative processes in the plasma. The first and second terms on the right hand side are the recombining- and ionizing-plasma components, respectively. Therefore, the transition rate into the 4^3S level owing to the recombination and excitation processes can be separately calculated by using the CR model.

Figures 15(a) and (b) show the logarithmic and linear plots for the P dependence of the recombining-plasma component $R_0(p)n_en_i$ and ionizing-plasma component $R_1(p)n_en_0$, calculated by using the CR model, where T_e and n_e, measured by using the TS in front of the target plate, were used for the CR model. The population density of the 4^3S level is more dominantly determined by the recombination component than the ionization component, throughout the presently considered range of pressures. This could explain why the low–n and high–n line emissions exhibit similar tendencies, as shown in figures 14(a) and (b). With increasing P, the ionizing component sharply decreases due to the significant loss of energetic electrons, and the recombination component exhibits a peak at $P \sim 9$ Pa, because the recombination process should be enhanced by the steep T_e reduction. After the peak, the recombination component decreases owing to the plasma extinction. The tendency of the recombination component calculated by using the CR model is consistent with the experimental result of high–n line emission in figure 14(b). It can be said that the optical emission observed in Pilot-PSI strongly depends on the plasma recombination processes under these experimental conditions such as the helium discharge and the low magnetic field of 0.05T.

4.6 Strong reduction of particle and heat fluxes due to EIR process

As a final part of the discussion, the parallel heat flux in detached recombining plasma in Pilot-PSI is

investigated. As explained in the section 1, the plasma heat flux q is simply described by eq. (1). Once $T_e << 3$ eV (E_i/γ') the heat flux to the target is dominated by the particle flux. Therefore, any further reductions in particle flux, likely due to EIR, but possibly other processes described in section 4.4, is essential to reduce parallel heat flux toward the divertor plate. Figures 16(a) and (b) show the particle flux and heat flux at the central region of plasma column, calculated by using the peak value of n_e and T_e measured by TS measurement in upstream ($z \sim 40$mm) and TS and single probe measurements in front of the target plate ($z \sim 540$mm). This might be considered equivalent to the estimation of heat flux reduction into the strike-point of a divertor plate. The particle flux Γ is calculated by the following formula,

$$\Gamma = 0.61 n_e (2T_e / m_i)^{1/2}. \quad (9)$$

Eq. (9) is different estimation from the $\phi_{measured}$ by using I_{sat} in DOD. The heat flux was calculated by eq. (1), where γ' and E_i were assumed to be 8 and 24.6 eV, respectively. As shown in figures 16(a) and (b), the particle and heat fluxes downstream dramatically decrease with P, while they are almost constant upstream. As with the above discussions, the momentum and energy losses increased with increasing P, leading to an enhancement of the EIR process. Thus, it can be said that EIR contribution to the reduction of particle and heat fluxes is increasing with P. At $P \sim 18$ Pa, the particle flux decreases from 10^{24} to 10^{22} $m^{-2}s^{-1}$ and heat flux from 7 MW/m^2 to 0.1 MW/m^2 between upstream and downstream regions, whose inter-distance is 0.5 m. The measured T_e at the plasma center was varied from 3 eV upstream to 0.2 eV downstream, and strong reduction of n_e from 10^{20} m^{-3} to 10^{19} m^{-3} was also observed along the magnetic field length, when $P \sim 18$ Pa. These results indicate more than 90% of particle and heat fluxes were dissipated in the short detached recombining plasma between the source and the target. The ion current losses are likely associated with recombination, but there are other processes described above in section 4.4. We have not quantitatively connected recombination to those ion current and power losses, the latter also affected by charge exchange and line emission. It is significant to investigate the reduction of heat flux at the plasma center under high particle flux ($\sim 10^{24}$ $m^{-2}s^{-1}$) conditions to aid predictions of the contribution of the EIR process to the detached divertor operation in fusion devices such as ITER. The stable control of the detached recombining plasma region is quite essential to reduce the heat load to the divertor plates.

5. Conclusion

In order to understand the fundamental properties of high-density and high-flux detached recombining helium plasma under the more ITER relevant conditions, T_e and n_e have been measured by using reciprocating electrostatic probes, TS measurement and OES in Pilot-PSI. In the present study, the

single probe properly showed the low T_e of less than 1 eV without any anomaly in recombining plasma, and T_e measured by using the electrostatic probes approximately corresponds to the TS measurement. The effect of plasma fluctuations is proposed as one of the explanations for incorrectly measured T_e by using electrostatic probes in other devices. Also, T_e was determined by using the Boltzmann plot method, using the emission from highly excited levels of helium atoms. It was shown that the T_e obtained by using OES was the lowest among all values obtained by using the measurement techniques considered in the present study, and exhibited only a small dependence on P. By comparing the plasma parameters in the upstream and downstream regions, the plasma column under the high neutral pressure condition exhibited a steep plasma pressure drop along the magnetic field lines, as well as a flux drop, estimated by the concept of DOD. This tendency was attributed to the momentum losses caused by processes such as EIR and charge-exchange. Based on the comparison between the population distributions obtained from the experiments and from the CR model calculations, we showed that the line emissions at $z \sim 540$ mm (in front of the target) owing to recombination process is strongly dominant over excitation there under Pilot-PSI experimental conditions. We also demonstrated that under high neutral pressure conditions (at $P \sim 18$Pa) the particle flux parallel to the magnetic field decreases from 10^{24} to 10^{22} $m^{-2}s^{-1}$ and parallel heat flux from 7 MW/m^2 to 0.1 MW/m^2, strongly correlating with, and likely due to recombination and charge exchange processes. These results indicated that more than 90% of particle and heat fluxes were dissipated in the short length of only 0.5 m in Pilot-PSI.

Acknowledgments

The authors would like to appreciate Mr. R.S. Al and Dr. K. Bystrov for skillful technical assistance and support in operation during the experiments in Pilot-PSI. This work was supported by JSPS KAKENHI Grant Number (25289337). This work is partially supported by NIFS/NINS under the project of Formation of International Network for Scientific Collaborations and NIFS Collaboration Research Program (NIFS14KUGM094).

References

[1] Eich T, Leonard A W, Pitts R A, Fundamenski W, Goldston R J, Gray T K, Herrmann A, Kirk A, Kallenbach A, Kardaun O, Kukushkin A S, LaBombard B, Maingi R, Makowski M A, Scarabosio A, Sieglin B, Terry J and Thornton A, ASDEX Upgrade team and JET EFDA Contributors 2012 *Proc. 24th Int. Conf. on Fusion Energy (San Diego, 2012)* ITR/1-1 http://www-naweb.iaea.org/napc/physics/FEC/FEC2012/index.htm

[2] Lipschultz B, Parra F I and Hutchinson I H 2016 *22nd PSI Conf. (Rome, Italy)* O-25

[3] Asakura N, Shimuzu K, Hoshino K, Tobita K, Someya Y, Utoh H, Nakamura M and Takizuka T 2012 *Proc. 24th Int. Conf. on Fusion Energy (San Diego, 2012)* ITR/1-1 http://www-naweb.iaea.org/napc/physics/FEC/FEC2012/index.htm

[4] Loarte A, Lipschults B, Kukushkin A S, Matthews G F, Stangeby P C, Asakura N, Counsell G F, Federici G, Kallenbach A, Krieger K, Mahdavi A, Philipps V, Reiter D, Roth J, Strachan J, Whyte D, Doerner R, Eich T, Fundamenski W, Herrimann A, Fenstermacher M, Ghendrih P, Groth M, Kirschner A, Konoshima S, LaBombard B, Lang P, Leonard A W, Monier-Garbet P, Neu R, Pacher H, Pegourie B, Pitts R A, Takamura S, Terry J, Tsitrone E and the ITPA Scrape-off Layer and Divertor Physics Topical Group, Progress in the ITER Physics Basis Chapter 4: Power and particle control 2007 *Nucl. Fusion* **47** S203

[5] Tobita K, Nishio S, Sato M, Sakurai S, Hayashi T, Shibama Y K, Isono T, Enoeda M, Nakamura H, Sato S, Ezato K, Hayashi T, Hirose T, Ide S, Inoue T, Kamada Y, Kawamura Y, Kawashima H, Koizumi N, Kurita G, Nakamura Y, Mouri K, Nishitani T, Ohmori J, Oyama N, Sakamoto K, Suzuki S, Suzuki T, Tanigawa H, Tsuchiya K and Tsuru D 2007 *Nucl. Fusion* **47** 892

[6] Tillack M S, Raffray A R, Wang X R, Malang S, Abdel-Khalik S, Yoda M and Youchison D 2001 *Fusion Eng. Des.* **86** 71

[7] Wischmeier M and The ASDEX Upgrade team and JET EFDA Contributions 2015 *J. Nucl. Mater.* **463** 22

[8] Asakura N, Shimizu K, Hoshino K, Tobita K, Tokunaga S and Takizuka T 2013 *Nucl. Fusion* **53** 123013

[9] Wiesen S, Groth M, Wischmeier M, Brezinsek S, JET contributors, The EUROfusion MST1team, The ASDEX Upgrade team, The Alcator C-mod team and The EAST team 2016 *22nd PSI Conf. (Rome, Italy)* R-02

[10] Takamura S, Ohno N, Nishijima D and Uesugi Y 2002 *Plasma Sources Sci. Technol.* **11** A42

[11] Hoshino K, Shimizu K, Takizuka T, Asakura N and Nakano T 2015 *J. Nucl. Mater.* **463** 573

[12] Doerner R, Temmerman G De and Ohno N "Contributions of Linear Plasma Devices to PMI Research" MPT/P7-29, paper presented at *25th IAEA Int. Conf. on Fusion Energy St. Petersburg 2014*

[13] Ohno N, Ezumi N, Takamura S, Krasheninnikov S I and Pigarov A Yu 1998 *Phys. Rev. Lett.* **81** 818

[14] Nishijima D, Ezumi N, Kojima H, Ohno N, Takamura S, Krasheninnikov S I and Pigarov A Yu 1999 *J. Nucl. Mater.* **266**–**269** 1161

[15] Nishijima D, Wenzel U, Ohsumi K, Ohno N, Uesugi Y and Takamura S 2002 *Plasma Phys. Control. Fusion* **44** 597

[16] Ezumi N, Ohno N, Aoki K, Nishijima D and Takamura S 1998 *Contrib. Plasma Phys.* **38** S31

[17] Ohno N, Tanaka N, Ezumi N, Nishijima D and Takamura S 2001 *Contrib. Plasma Phys.* **41** 473

[18] Tanaka H, Ohno N, Tsuji Y and Kajita S 2010 *Contrib. Plasma Phys.* **50** 256

[19] Tanaka H, Ohno N, Tsuji Y, Okazaki K and Kajita S 2012 *Contrib. Plasma Phys.* **52** 424

[20] Kado S, Kobayashi H, Oishi T and Tanaka S 2003 *J. Nucl. Mater.* **313**–**316** 754

[21] Okamoto A, Kado S, Kajita S and Tanaka S 2005 *Rev. Sci. Instrum.* **76** 116106

[22] Kado S, Suzuki K, Iida Y and Muraki A 2011 *J. Nucl. Mater.* **415** S1174

[23] Tanaka S, Iijima T, Tonegawa A, Kawamura K and Sato K N 2013 *Fusion Sci. Technol.* **63** 420

[24] Ono M, Tonagewa A, Kumita K, Yazawa H, Shibuya T and Kawamura K 2006 *J. Plasma Fusion Res.* **7** 50

[25] Hollmann E M, Pigarov A Yu and Yan S 2007 *J. Nucl. Mater.* **363**–**365** 359

[26] Hollmann E M, Brandt C, Hudson B, Kumar D, Nishijima D and Pigarov Yu 2013 *Phys. Plasmas* **20** 093303

[27] Campbell D J and Domestic Agencies and ITER collaborators 2012 *Proc. 24th Int. Conf. on Fusion Energy (San Diego, 2012)* ITR/1-1 http://www-naweb.iaea.org/napc/physics/FEC/FEC2012/index.htm

[28] Bardin S, Morgan T W, Glad X, Pitts R A and Temmerman G De 2015 *J. Nucl. Mater.* **463** 193

[29] Lee H T, Temmerman G De, Gao L, Schwarz–Selinger T, Meisl G, Höschen T and Ueda Y 2015 *J. Nucl. Mater*. **463** 974

[30] Wright G M, Mayer M, Ertl K, de Saint–Aubin G and Rapp J 2010 *Nucl. Fusion* **50** 075006

[31] Temmerman G De, Zielinski J J, van Diepen S, Marot L and Price M 2011 *Nucl. Fusion* **51** 073008

[32] Vijvers W A J, Al R S, Lopes Cardozo N J, Goedheer W J, de Groot B, Kleyn A W, van der Meiden H J, can de Peppel R J E, Schram D C, Shumack A E, Westerhout J and van Rooij G J 2007 *Proc. 28th Int. Conf. on Phenomena in Ionized Gases (Prague, Czech Republic)* 4P11-15

[33] Monk R D, Loarte A, Chankin A, Clement S, Davies S J, Günther K, Guo H Y, Lingertat J, Maggi C F, Matthews G F, Morgan P D, Stamp M F and Tabasso A 1996 *Contrib. Plasma Phys.* **36** 37

[34] Monk R D, Loarte A, Chankin A, Clement S, Davies S J, Ehrenberg J K, Guo H Y, Lingertat J,

Matthews G F, Stamp M F and Stangeby P C 1997 *J. Nucl. Mater.* **241** 396

[35] Batishchev O V, Krasheninnikov S I, Catto Peter J, Batishcheva A A, Sigmar D J, Xu X Q, Byers J A, Rognlien T D, Cohen R H, Shoucri M M and Shkarofskii I P 1997 *Phys. Plasmas* **4** 1672

[36] Okamoto A, Kado S, Iida Y and Tanaka S 2006 *Contrib. Plasma Phys.* **46** 416

[37] van Rooij G J, Veremiyenko V P, Goedheer W J, de Groot B, Kleyn A W, Smeets P H M, Versloot T W, Whyte D G, Engeln R, Schram D C, and Lopes Cardozo N J 2007 *Appl. Phys. Lett.* **90** 121501

[38] Ohno N, Nishijima D, Takamura S, Uesugi Y, Motoyama M, Hattori N, Arakawa H, Ezumi N, Krasheninnikov S, Pigarov A and Wenzel U 2001 *Nucl. Fusion* **41** 1055

[39] Kukushkin A S, Pacher H D, Loarte A, Komarov V, Kotov V, Merola M, Pacher G W and Reiter D 2009 *Nucl. Fusion* **49** 075008

[40] Ohno N, Furuta K and Takamura S 2004 *J. Plasma Fusion Res.* **80** 275

[41] Hayashi Y, Nishikata H, Ohno N and Kajita S 2016 *Plasma Fusion Res.* **11** 1202005

[42] van der Meiden H J, Al R S, Barth C J, Donné A J H, Engeln R, Goedheer W J, de Groot B, Kleyn A W, Koppers W R, Lopes Cardozo N J, van de Pol M J, Prins P R, Schram D C, Shumack A E, Smeets P H M, Vijvers W A J, Westerhout J, Wright G M and van Rooij G J 1 SEP 2008 *Rev. Sci. Instrum.* **79** 013505

[43] van Rooij G J, van der Meiden H J, 't Hoen M H J, Koppers W R, Shumack A E, Vijvers W A, Westerhout J, Wright G M and Rapp J 2009 *Plasma Phys. Control. Fusion* **51** 124037

[44] Barth C J, Chu C C, Beurskens M N A and van der Meiden H J 2001 *Rev. Sci. Instrum.* 72 3514

[45] Ohno N, Tanaka M, Ezumi N, Nishijima D, Takamura S, Krasheninnikov S I, Pigarov A Yu and Park J 1999 *Phys. Plasmas* **6** 2486

[46] Hayashi Y, Ohno N, Kajita S and Tanaka H 2016 *Phys. Plasmas* **23** 012511

[47] Antar G Y, Krasheninnikov S I, Devynck P, Doerner R P, Hollmann E M, Boedo J A, Luckhardt S C and Conn R W 2001 *Phys. Rev. Lett.* **87** 065001

[48] Carter T A 2006 *Phys. Plasmas* **13** 010701

[49] Antar G Y, Counsell G, Yu Y and Devynck P 2003 *Phys. Plasmas* 2003 **10** 419

[50] Krasheninnikov S I 2001 *Phys. Lett. A* **283** 268

[51] Grulke O, Terry J L, LaBombard B and Zweben S J 2006 *Phys. Plasmas* **13** 012306

[52] Krasheninnikov S I and Smolyakov A I 2003 *Phys. Plasmas* **10** 3020

[53] Kajita S, Ohno N, Takamura S and Nakano T 2006 *Phys. Plasmas* **13** 013301

[54] Vijvers W A J, van Gils C A J, Goedheer W J, van der Meiden H J, Schram D C, Veremiyenko V P, Westerhout J, Lopes Cardozo N J and van Rooij G J 2008 *Phys. Plasmas* **15** 093507

[55] Wesson J, Campbell D J, Connor J W, Gill R D and Hawkes N C 2004 *Tokamaks 3rd edition*

(Oxford: Oxford Univ. Press)

[56] Stangeby P C 2000 *The Plasma Boundary of Magnetic Fusion Devices* (London: Institute of Physics Publishing)

[57] Loarte A, Monk R D, Martin–Solis J R, Campbell D J, Chankin A V, Clement S, Davies S J, Ehrenberg J, Erents S K, Guo H Y, Harbour P J, Horton L D, Ingesson L C, Jäckel H, Lingertat J, Lowry C G, Maggi C F, Matthews G F, McCormick K, O'Brien D P, Reichle R, Saibene G, Smith R J, Stamp M F, Stork D and Vlases G C 1998 *Nucl. Fusion* **38** 331

[58] Horton L D, Vlases G C, Andrew P, Bhatnagar V P, Chankin A V, Clement S, Conway G D, Davies S J, de Haas J C M, Ehrenberg J K, Fishpool G M, Gauthier E, Guo H Y, Harbour P J, Ingesson L C, Ja¨ckel H J, Lingertat J, Loarte A, Lowry C G, Maggi C F, Matthews G F, McCracken G M, Mohanti R, Monk R D, Reichle R, Righi R, Saibene G, Sartori R, Simonini R, Stamp M F, Taroni A and Thomsen K 1999 *Nucl. Fusion* **39** 1

[59] Ohno N, Mori S, Ezumi N, Takagi M and Takamura S 1996 *Contrib. Plasma Phys.* **36** 339

[60] Ezumi N, Mori S, Ohno N, Takagi M, Takamura S, Suzuki H and Park J 1997 *J. Nucl. Mater.* **241**–**243** 349

[61] Goto M, Sawada K, Fujimoto T 2002 *Phys. Plasmas* **9** 4316

[62] Goto M 2003 *J. Quant. Spectrosc. Radiat. Transf.* **76** 331

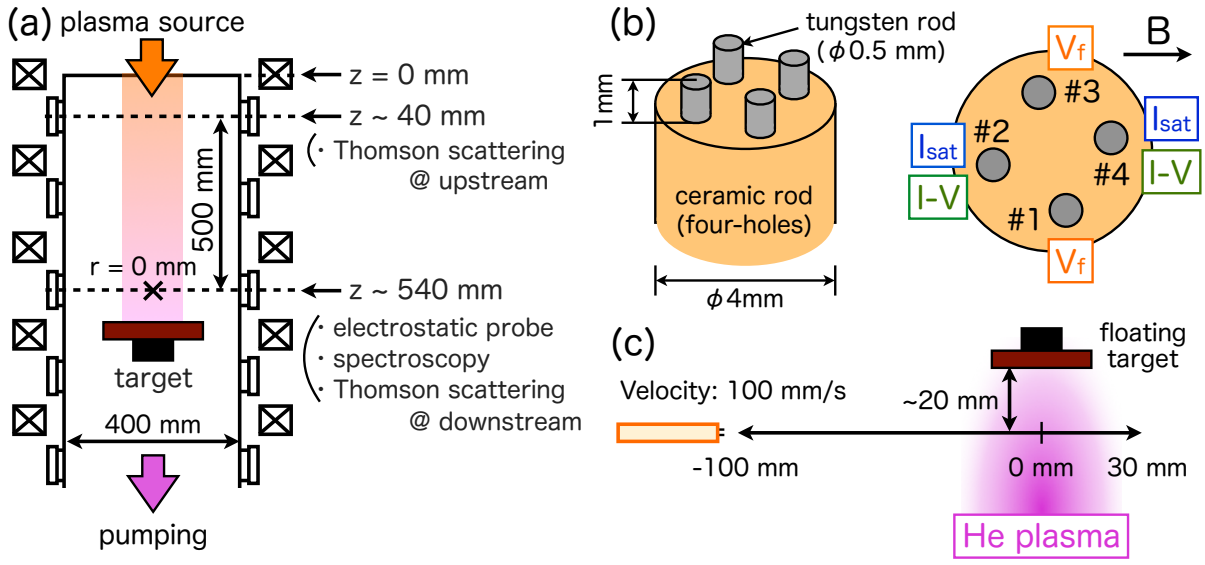

Figure 1. (a) Schematic top view of the Pilot-PSI system, (b) a schematic of the electrostatic probe head designed for the single probe, the double probe, and the measurements of I_{sat} and V_f, and (c) the movement of the probe into the plasma, approximately 20 mm in front of the target. The electrostatic probe measurement, TS measurement and OES were performed downstream (z ~ 540 mm). TS measurement was also carried out upstream (z ~ 40 mm). (Double column)

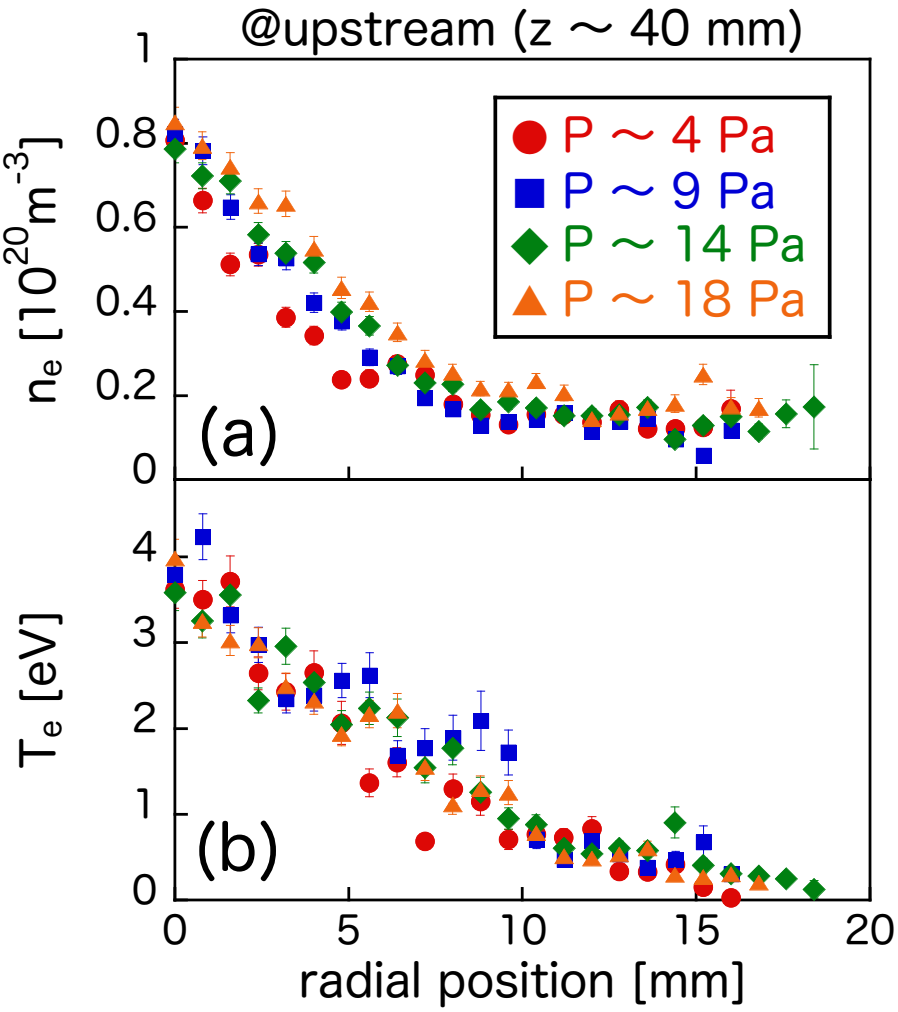

Figure 2. Radial profiles of (a) n_e and (b) T_e for various P, measured by using the TS measurement at z ~ 40 mm. (Single column)

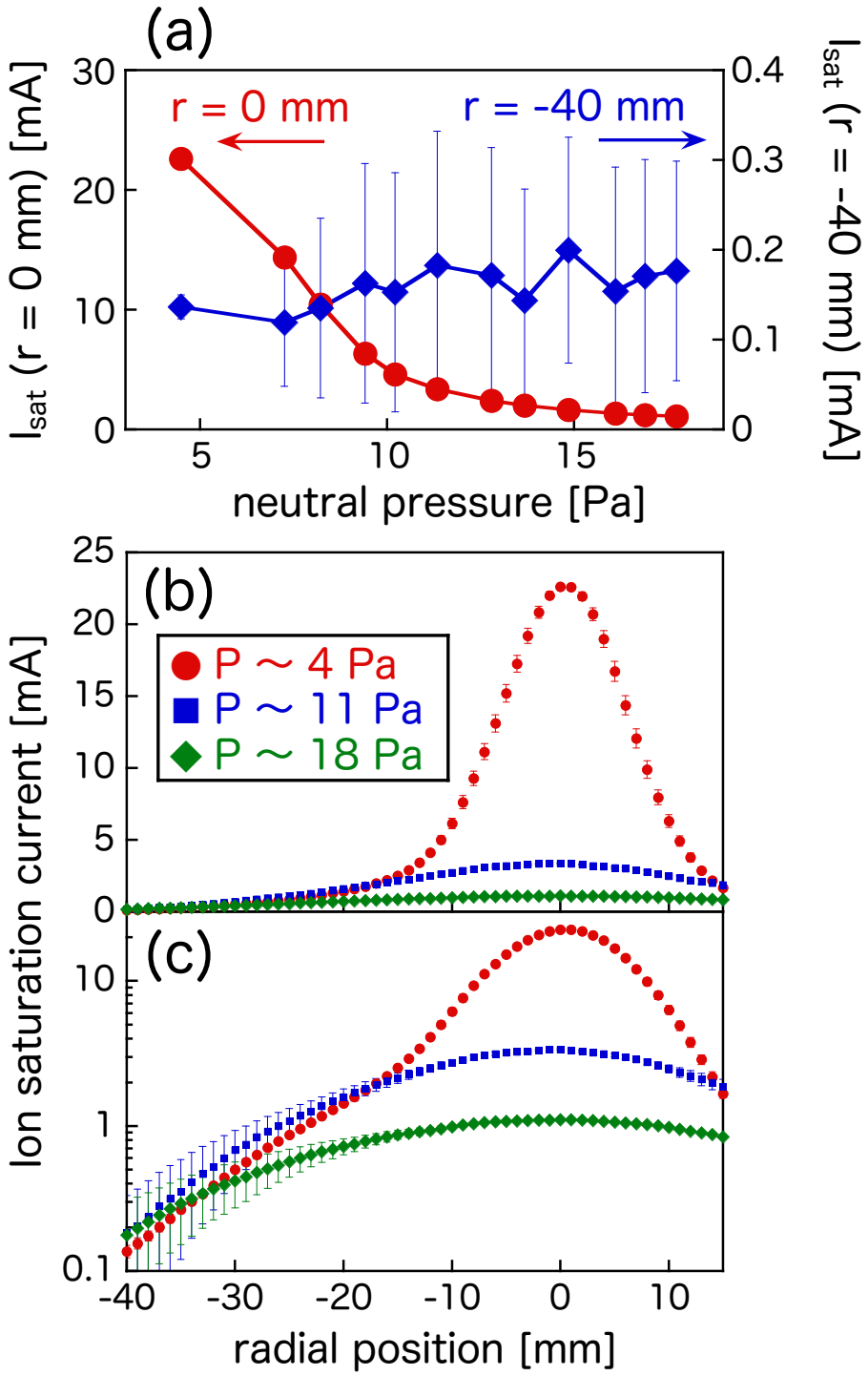

Figure 3. (a) Neutral pressure dependence of I_{sat} measured at the plasma center (r = 0 mm) and plasma edge (r = –40 mm), and (b) linear and (c) logarithmic plots of I_{sat} radial profiles for the pressures of approximately 4, 11, and 18 Pa. The error bars represent the standard deviation of I_{sat}. (Single column)

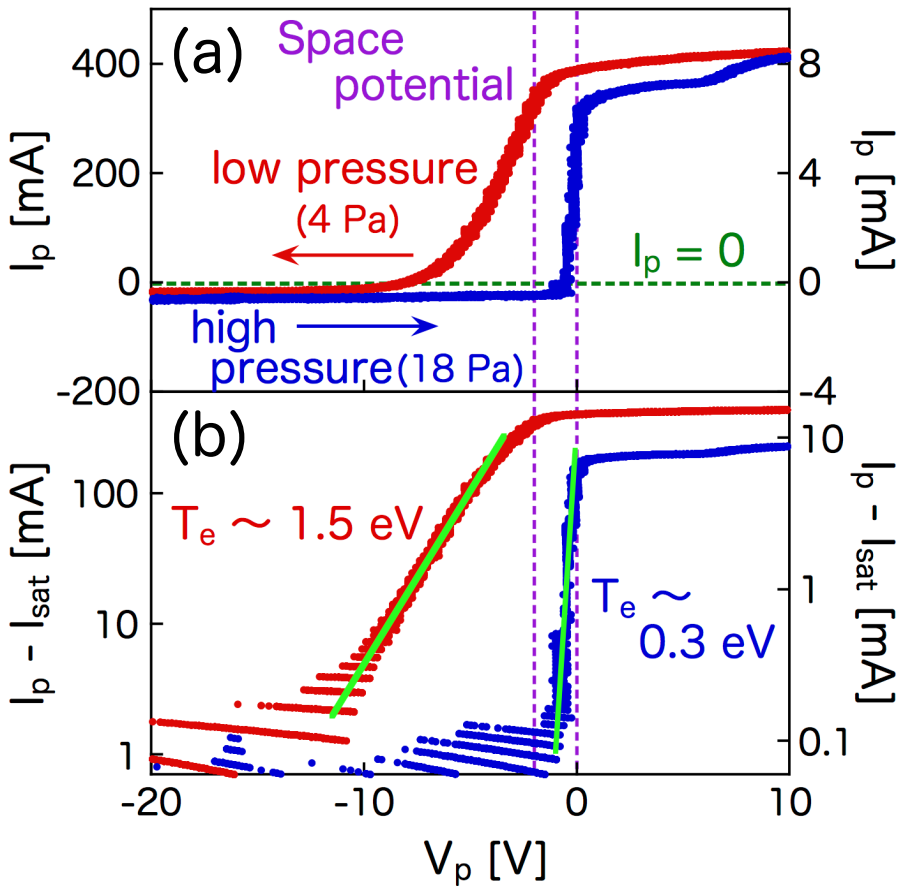

Figure 4. Comparison between the *I-V* characteristics of the single probe measured at $r = 0$ mm at the lowest and highest considered pressures. (a) The probe current on the linear scale and (b) the electron current on the logarithmic scale, for estimation of T_e. (Single column)

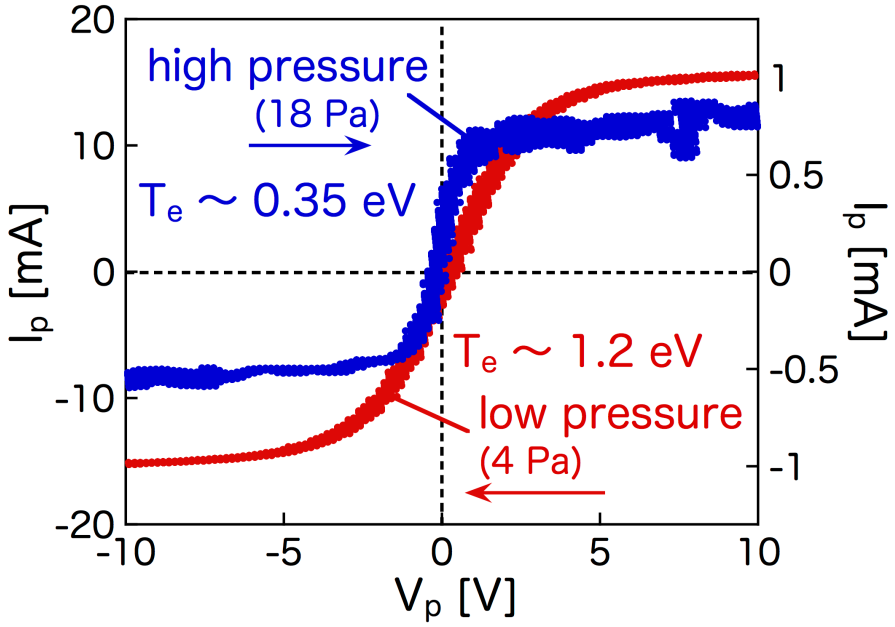

Figure 5. Comparison between the *I-V* characteristics of the double probe, measured at $r = 0$ mm at the lowest and highest considered pressures. (Single column)

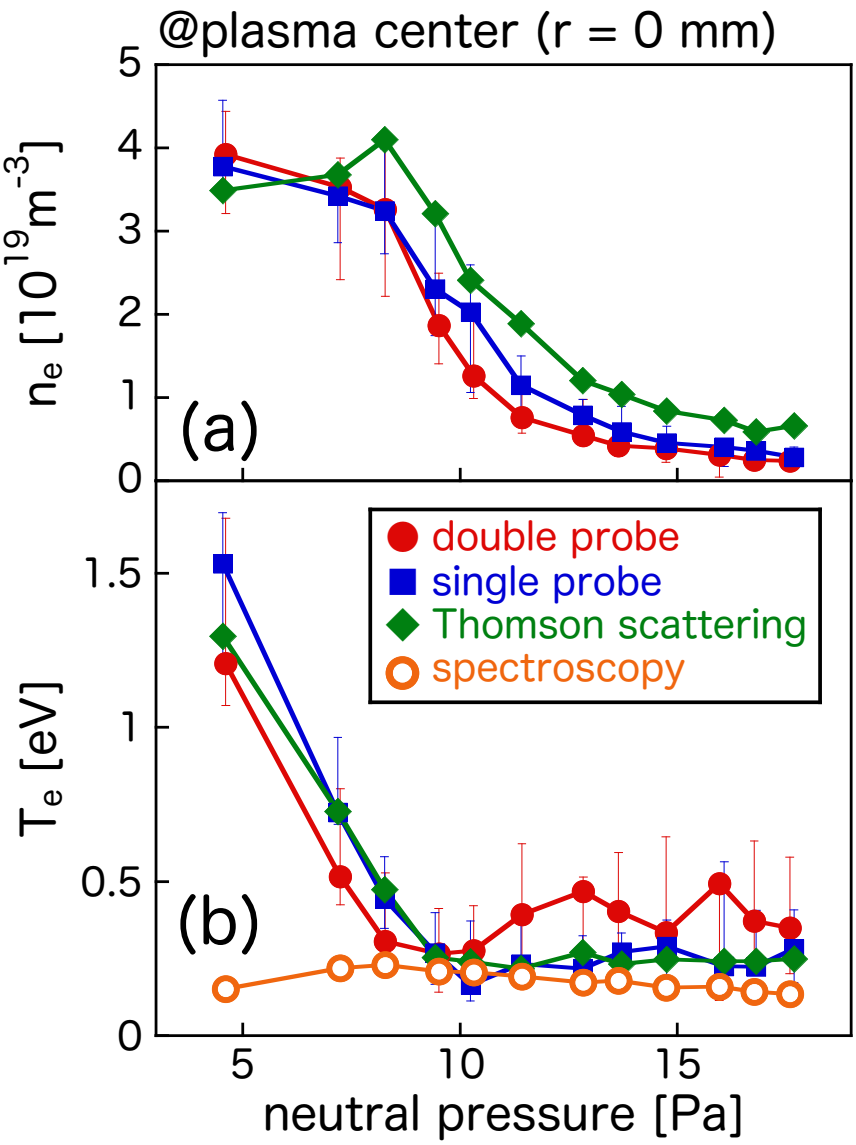

Figure 6. Neutral pressure dependence of (a) n_e and (b) T_e measured at the plasma center by using the double probe, the single probe, the TS, and spectroscopy at $z \sim 540$ mm. The error bars represent the analytical error in the T_e estimation by fitting for the probes and errors for TS measurements were determined from the least mean square fit (error is inversely proportional to square root of the number of photoelectrons collected at the photocathode of the intensified CCD camera) [44]. (Single column)

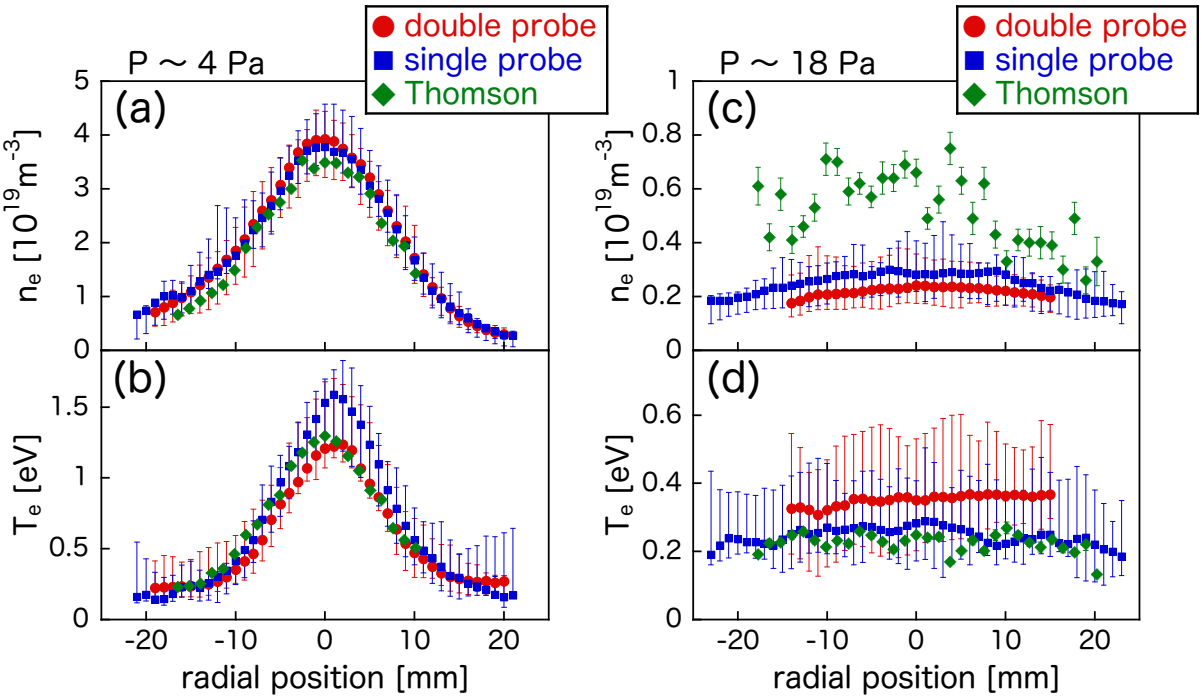

Figure 7. Radial profiles of (a) n_e and (b) T_e for $P \sim 4$ Pa and (c) n_e and (d) T_e for $P \sim 18$ Pa, measured by using the double probe, the single probe and the TS measurements at z ~ 540 mm. (Double column)

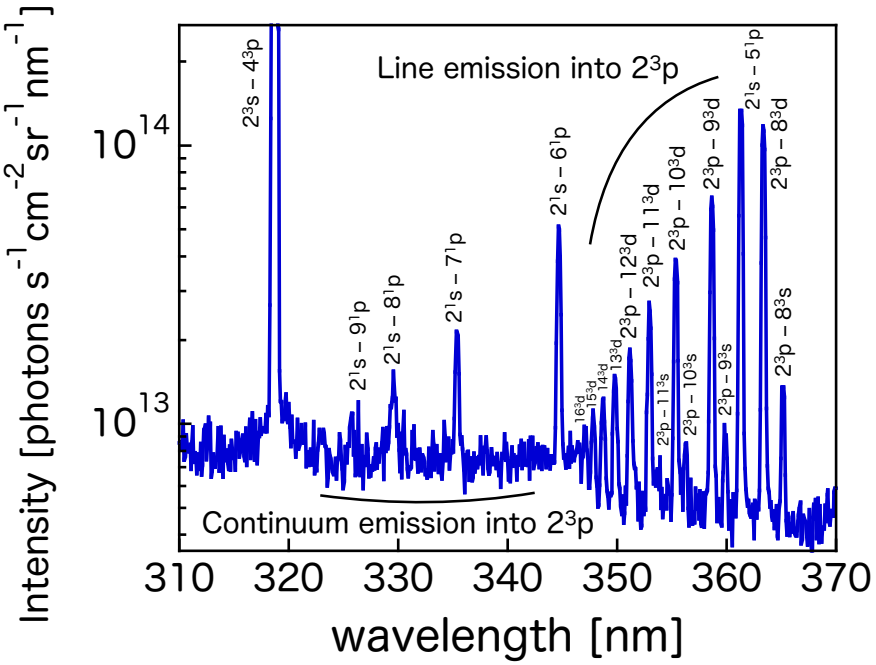

Figure 8. Visible light emission spectra from helium recombining plasma at $P \sim 9$ Pa. (Single column)

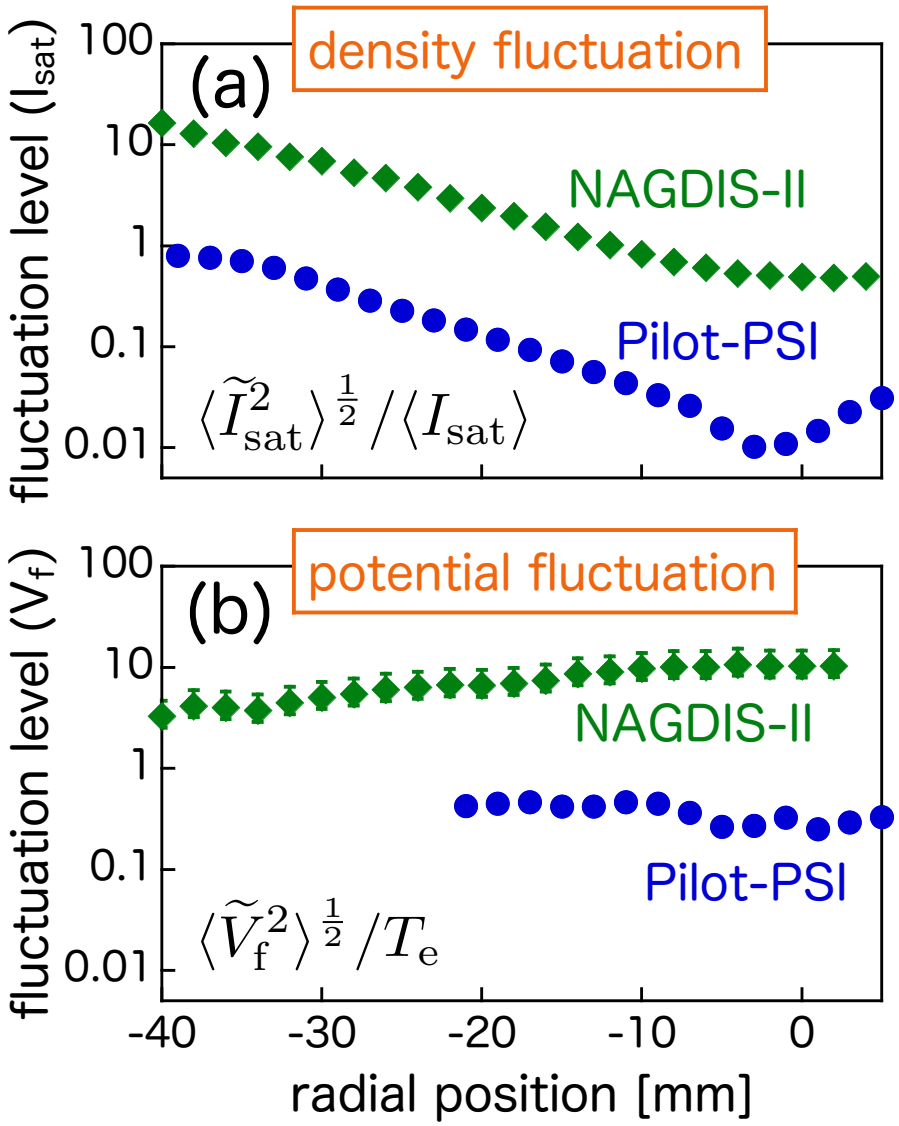

Figure 9. Radial profiles of fluctuation levels of I_{sat} (a) and V_f (b) measured in typical detached recombining plasmas in NAGDIS-II and Pilot-PSI. Standard deviations of I_{sat} and V_f were normalized by averaged I_{sat} and T_e, respectively. In NAGDIS-II, T_e was assumed to be 0.5 eV, having the ± 30% errors. (Single column)

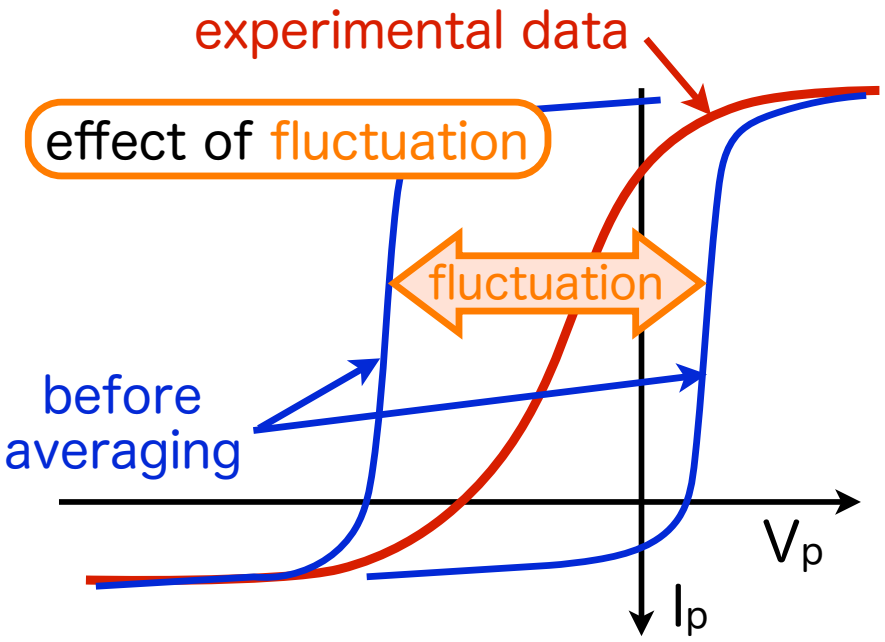

Figure 10. Effect of plasma potential fluctuation on the single probe *I-V* characteristics, when the amplitude of plasma potential fluctuation is larger than T_e. (Single column)

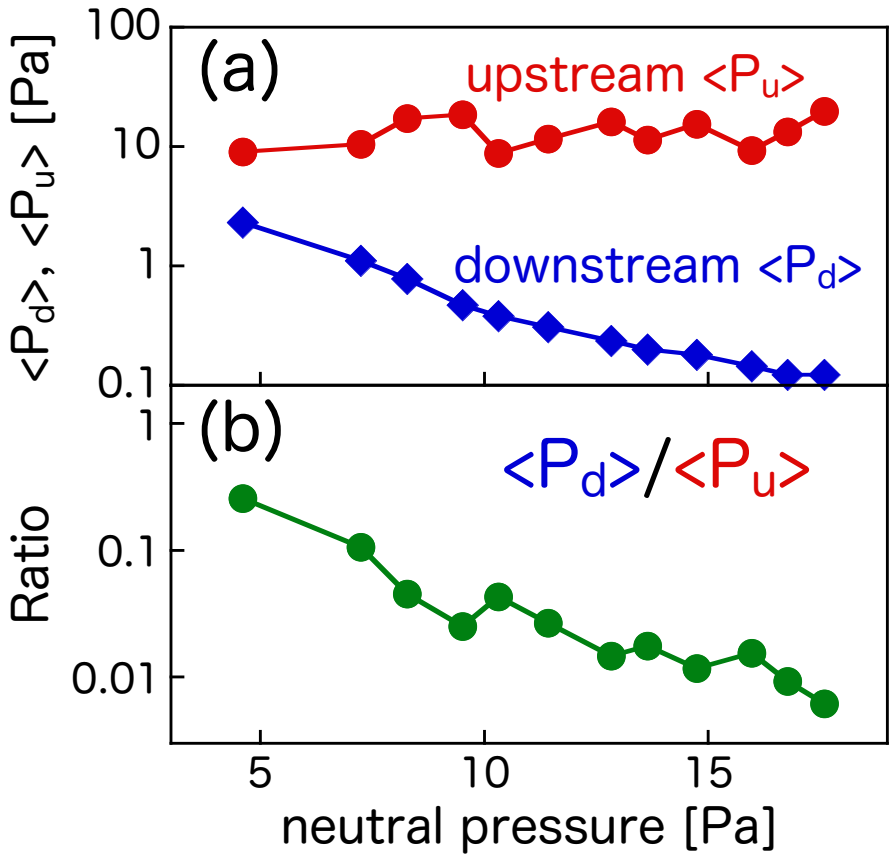

Figure 11. Neutral pressure dependence of plasma pressure (a), estimated as radially-averaged $n_e T_e$ at different positions (z ~ 40 and 540 mm) along the magnetic field lines, and the ratio (b). (Single column)

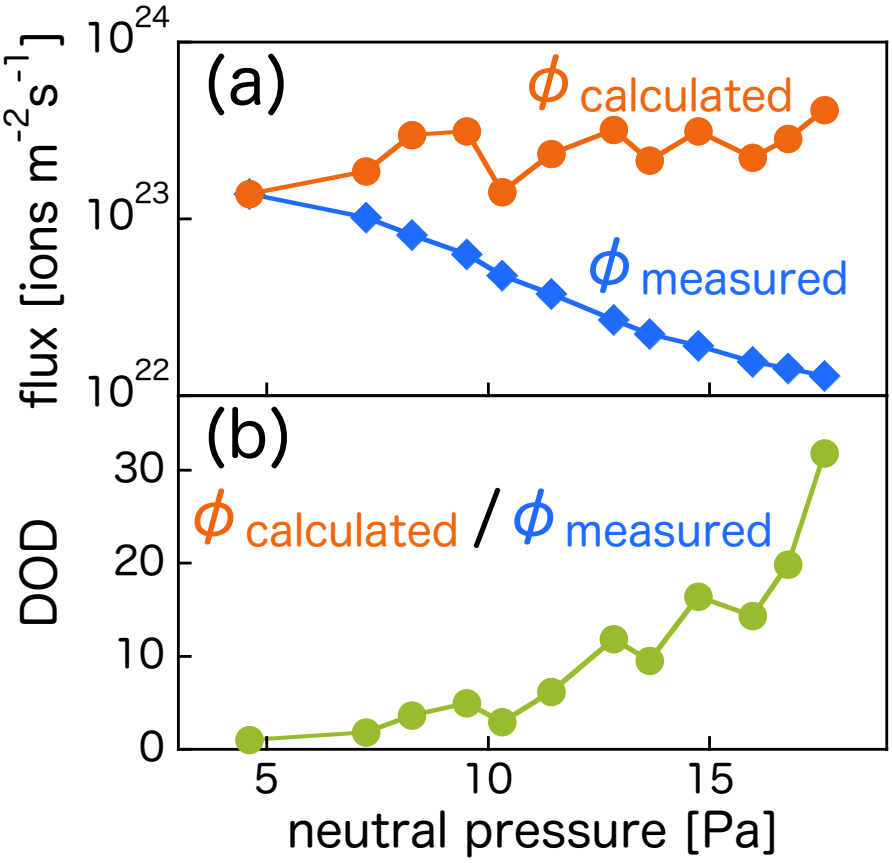

Figure 12. Neutral pressure dependence of $\phi_{calculated}$, $\phi_{measured}$ (a) and DOD (b). (Single column)

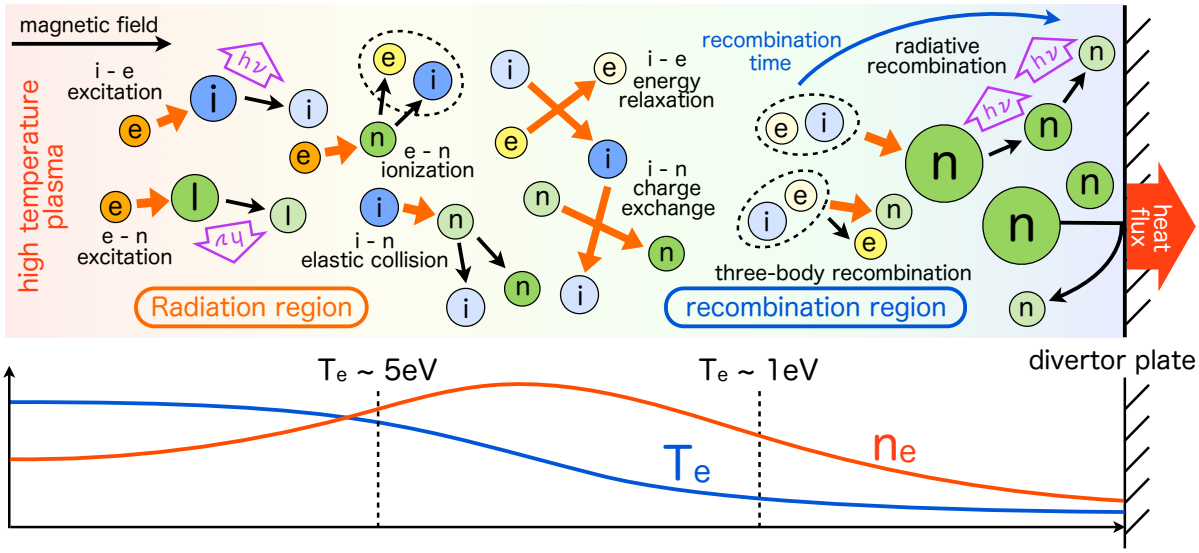

Figure 13. Schematic illustration of the formation of detached helium plasma and axial profiles of n_e and T_e during the transport into the divertor plate under high neutral pressure conditions, where the divertor plasma in a fusion device is assumed. The labels ‘e’, ‘i’, ‘n’ and ‘I’ indicate ‘electron’, ‘ion’, ‘neutral helium’ and ‘impurity’, respectively. The large bubbles correspond to highly excited atoms, and the color shows the energy. (Double column)

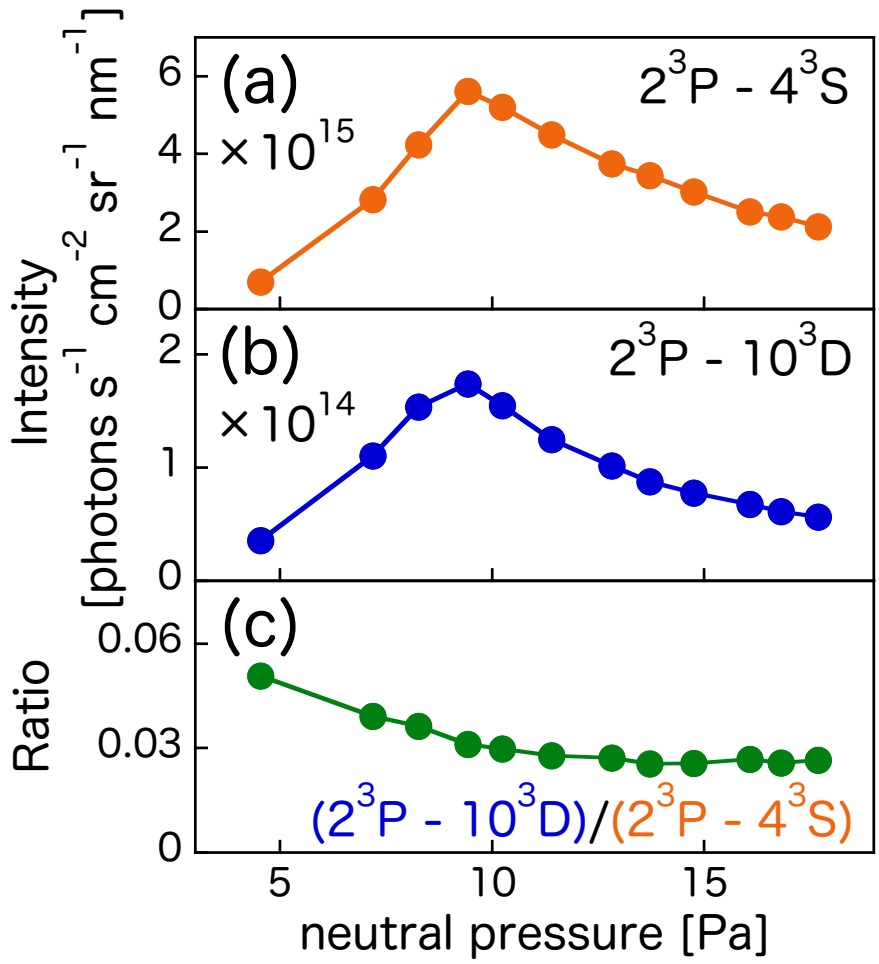

Figure 14. Neutral pressure dependence of the low–*n* He–I (471.3 nm: 2^3p–4^3s) emission (a), the high–*n* He–I (355.4 nm: 2^3p–10^3d) emission (b), and the ratio of 471.3/355.4 nm (c). (Single column)

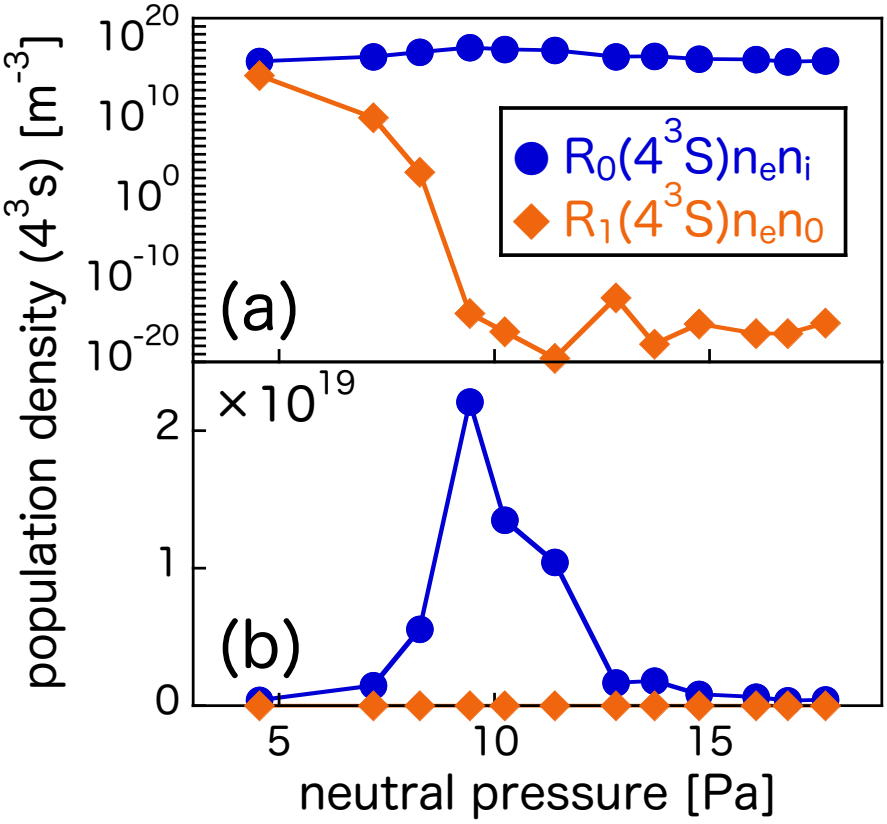

Figure 15. Logarithmic (a) and linear (b) plots for neutral pressure dependence of the recombining plasma component $R_0(p)n_en_i$ and the ionizing plasma component $R_1(p)n_en_0$, calculated by using the CR model. (Single column)

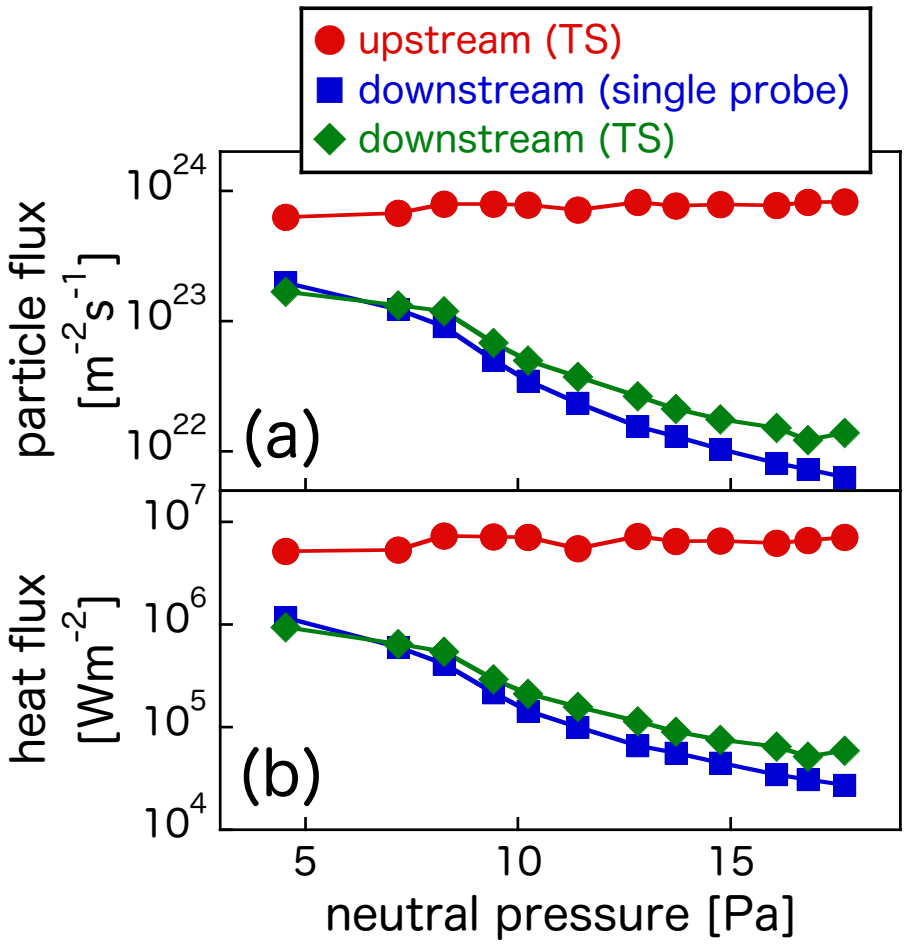

Figure 16. Neutral pressure dependence of particle (a) and heat (b) fluxes calculated upstream ($z \sim 40$ mm) and downstream ($z \sim 540$ mm). Particle flux is $\Gamma = 0.61 n_e (2T_e/m_i)^{1/2}$, and heat flux is $q = \Gamma[\gamma' T_e + E_i]$, where γ' was assumed to be 8 and E_i to be 24.6 eV. Downstream, Γ and q calculated by using results measured by both TS and single probe are shown. (Single column)